The Meteoritical Society

Meteoritics & Planetary Science 1–15 (2019)
doi: 10.1111/maps.13286

Shock-induced phase transformation of anorthitic plagioclase in the eucrite meteorite Northwest Africa 2650

De-Liang CHEN[1], Ai-Cheng ZHANG[1,2*], Run-Lian PANG[1], Jia-Ni CHEN[1], and Yang LI[3]

[1]State Key Laboratory for Mineral Deposits Research, School of Earth Sciences and Engineering, Nanjing University, Nanjing 210023, China
[2]CAS Center for Excellence in Comparative Planetology, Hefei 230026, China
[3]Institute of Geochemistry, Chinese Academy of Sciences, Guiyang 550081, China
*Corresponding author. E-mail: aczhang@nju.edu.cn

(Received 10 January 2019; revision accepted 04 March 2019)

Abstract–Anorthite is an important constituent mineral in basaltic achondrites from small celestial bodies. Its high-pressure phase transformation in shocked meteorites has not been systematically studied. In this study, we report the diverse phase transformation behaviors of anorthite in a shocked eucrite Northwest Africa (NWA) 2650, which also contains coesite, stishovite, vacancy-rich clinopyroxene, super-silicic garnet, and reidite. Anorthite in NWA 2650 has transformed into anorthite glass (anorthite glassy vein, maskelynite, and glass with a schlieren texture and vesicles), tissintite and dissociated into three-phase assemblage grossular + kyanite + silica glass. Different occurrences of anorthite glass might have formed via the mechanism involving shear melting, solid-state transformation, and postshock thermally melting, respectively. Tissintite could have crystallized from a high-pressure plagioclase melt. The nucleation of tissintite might be facilitated by relict pyroxene fragments and the early formed vacancy-rich clinopyroxene. The three-phase assemblage grossular, kyanite, and silica glass should have formed from anorthitic melt at high-pressure and high-temperature conditions. The presence of maskelynite and reidite probably suggests a minimum peak shock pressure up to 20 GPa, while the other high-pressure phases indicate that the shock pressure during the crystallization of shock melt veins might vary from >8 GPa to >2 GPa with a heterogeneous temperature distribution.

INTRODUCTION

Shock metamorphism is a fundamental and important process in the evolution of the planets and asteroids in the solar system. Minerals may have transformed into their high-pressure polymorphs and glasses or dissociated into multiphase assemblages under shock-induced high-pressure and high-temperature conditions. In the past two decades, high-pressure phase transformation of mafic minerals in shocked meteorites has been extensively investigated (Sharp and DeCarli 2006; Gillet and El Goresy 2013; Tomioka and Miyahara 2017; Ma 2018). However, phase transformation of feldspar minerals (especially K-feldspar and anorthite) in natural shocked samples was less studied, compared to mafic silicate minerals (olivine and pyroxene) (e.g., Ma et al. 2018). This is probably due to the relatively rare occurrence of K-feldspar and anorthite in highly shocked ordinary chondrites and Martian meteorites. Recently, tissintite and stöfflerite, two high-pressure polymorphs of labrodorite, have been found in shocked Martian meteorites (Walton et al. 2014; Ma et al. 2015; Tschauner and Ma 2017; Sharp et al. 2019). In addition, tissintite has also been observed in the shocked eucrite Northwest Africa 8003 (Pang et al. 2016). The recent high-pressure experimental investigations of plagioclase (e.g., Kubo et al. 2010; Jaret et al. 2015; Rucks et al. 2018; Sims et al. 2019) and the observations of different plagioclase polymorphs in shocked samples have improved our understanding of the phase transformation behaviors, mechanisms, and conditions of anorthitic plagioclase.

While studying the shock metamorphism of the howardite-eucrite-diogenite (HED) clan meteorites, we

observed various phase transformation phenomena of anorthitic plagioclase in a shocked eucrite Northwest Africa (NWA) 2650. In this study, we report the mineralogical features of NWA 2650 and specifically concentrate on the diverse phase transformation behaviors and mechanisms of anorthitic plagioclase.

SAMPLE AND ANALYTICAL METHODS

Northwest Africa 2650 is a brecciated eucrite that was purchased in Erfoud, Morocco. It is classified as a monomict eucrite and has a total weight of 2.22 kg (Meteoritcal Bulletin 2018). Five polished sections of NWA 2650 were investigated in this study.

Petrographic texture of NWA 2650 was observed using two scanning electron microscopes (SEM; JEOL JSM-6490 and Zeiss supra 55) instruments at Nanjing University, China. Both instruments were operated in backscattered electron (BSE) imaging mode at an accelerating voltage of 15 kV.

Chemical compositions of minerals and glass in this study were mainly determined using a JEOL 8100 electron probe micro-analyzer (EPMA) equipped with four wavelength dispersive spectrometers (WDS) at Nanjing University. Measurements of most minerals were performed with a focused beam (1–2 μm in diameter) of 20 nA, accelerated at 15 kV. Natural and synthetic standards were used to calibrate the contents of Si, Ti, Al, Cr, Fe, Mn, Mg, Ca, Na, and K. All compositions were reduced with the ZAF correction procedure for the JEOL microprobe instrument.

Structural characterization of minerals in NWA 2650 was performed using electron backscatter diffraction (EBSD), laser Raman spectroscopy, and transmission electron microscopy (TEM). The EBSD patterns of minerals were obtained using an Oxford EBSD detector attached to the JEOL 7000F Field-Emission-Gun SEM instrument at Hokkaido University, Japan. The SEM instrument was operated with an accelerating voltage of 20 kV and a beam current of 4 nA. Before obtaining EBSD patterns, the sample was polished with silica suspension and carbon-coated. The obtained EBSD patterns of minerals were indexed using their potential polymorphs. The indexing quality is estimated based on the mean angular deviation (MAD) value. In this study, MAD values of less than 0.5 are considered desirable for accurate solutions.

Raman spectra were obtained with the laser micro-Raman spectrometer Reinshaw RM2000 at Nanjing University. An optical microscope (×500) was used to focus the excitation laser beam of 514 nm (Ar^+ laser) on the target phases. Measurements were performed with a laser power of ~5 mW and a spot size of ~2–3 μm. The identification of minerals is based on the comparison with online database (www.rruff.info).

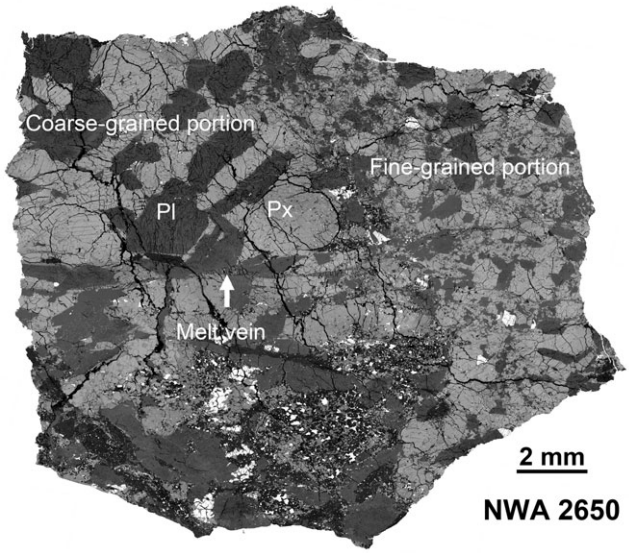

Fig. 1. Mosaic backscattered electron image of a polished section of the NWA 2650 meteorite. The meteorite contains a coarse-grained portion and a fine-grained portion. In the middle part of this section, melt veins cut both coarse-grained and fine-grained portions continuously. Px = pyroxene; Pl = plagioclase.

A thin foil containing grossular and kyanite was prepared with a FEI Scios focused ion beam (FIB) system at the Institute of Geochemistry, Guiyang, China. The thin foil is approximately 100 nm in thickness after being extracted and thinned at various accelerating voltages and beam currents, the cutting and thinning conditions are the same to that in Wang et al. (2019). The FIB foil was observed with a FEI Tecnai F20 TEM instrument at Nanjing University at both high-angle annual dark field scanning transmission electron microscopy (HAADF-STEM) and bright field TEM modes. An accelerating voltage of 200 kV was used. Qualitative chemical compositions of phases in the FIB foil were determined with an energy dispersive X-ray spectrometer (EDS) attached on the F20 TEM instrument. Elemental mapping was performed to reveal the distribution of elements at given regions. The phases in the FIB foil was identified by combining EDS measurements, high-resolution TEM imaging with fast Fourier transformation (FFT), and selected area electron diffraction (SAED).

RESULTS

Northwest Africa 2650 contains mainly two portions of various grain sizes (Fig. 1). Both portions contain pyroxene and plagioclase as the major

Table 1. Average compositions of pyroxene grains in the host rock of NWA 2650.

	Coarse-grained portion				Fine-grained portion			
	Orthopyroxene		Augite		Orthopyroxene		Augite	
	Average (n = 6)	1SD	Average (n = 7)	1SD	Average (n = 6)	1SD	Average (n = 6)	1SD
SiO_2	49.9	0.40	51.0	0.06	49.6	0.36	51.2	0.29
TiO_2	0.15	0.03	0.31	0.05	0.11	0.01	0.23	0.06
Cr_2O_3	0.07	0.02	0.22	0.02	0.06	0.03	0.17	0.02
Al_2O_3	0.16	0.02	0.65	0.01	0.13	0.03	0.50	0.06
FeO	35.0	0.38	16.3	0.20	35.8	0.32	16.3	0.35
MnO	1.15	0.03	0.54	0.03	1.18	0.03	0.54	0.01
MgO	12.1	0.17	10.1	0.19	12.3	0.21	10.3	0.03
CaO	1.63	0.32	21.0	0.15	0.85	0.16	21.0	0.40
Na_2O	bdl		0.08	0.03	bdl		0.06	0.02
Total	100.2		100.2		100.0		100.3	
Si	1.992		1.968		1.986		1.972	
Ti	0.004		0.009		0.003		0.007	
Cr	0.002		0.007		0.002		0.005	
Al	0.008		0.029		0.006		0.023	
Fe	1.168		0.524		1.200		0.523	
Mn	0.039		0.018		0.040		0.018	
Mg	0.717		0.578		0.731		0.589	
Ca	0.069		0.869		0.037		0.868	
Na	bdl		0.006		0.001		0.004	
Sum	4.000		4.008		4.007		4.010	
Fe/Mn	30.0		29.6		29.9		29.7	
En	36.7		29.3		37.2		29.8	
Fs	59.8		26.6		61.0		26.4	
Wo	3.5		44.1		1.9		43.8	

Bdl = below detection limit.
The cations are calculated based on six oxygen atoms.

constituent phases. Minor minerals in this meteorite include chromite, ilmenite, quartz, Ca-phosphate (merrillite and apatite), zircon, and troilite as late-stage phases. Iron-nickel metal grains are also observed. All pyroxene grains in the two portions show augite exsolution lamellae (usually 2–20 μm in width) within Fe-rich orthopyroxene. The compositional ranges of orthopyroxene and augite in the coarse-grained portion are $En_{35.4–37.8}Fs_{56.9–62.1}Wo_{1.9–6.4}$ and $En_{28.7–29.8}Fs_{26.2–27.1}Wo_{43.5–44.4}$, respectively. The compositions of orthopyroxene ($En_{36.7–37.8}Fs_{60.0–61.7}Wo_{1.5–2.8}$) and augite ($En_{29.5–30.2}Fs_{25.7–27.5}Wo_{42.8–44.6}$) in the relatively fine-grained portion show overlapping with those in the coarse-grained portion (Table 1). The average Fe/Mn value of pyroxene is 30, which is consistent with those of pyroxenes in other HED meteorites (McSween et al. 2011). The An values of plagioclase in the coarse-grained and fine-grained portions are 82–92 and 81–92, respectively. The overlapping compositions of anorthite and pyroxene in both portions, suggest a common source for them, indicating that NWA 2650 is a monomict breccia. Based on the compositions of orthopyroxene and augite, the host rock of NWA 2650 should have experienced an equilibrium temperature of 814 ± 33 °C (Brey and Köhler 1990).

Shock-induced melt veins are commonly observed in NWA 2650. Some of the melt veins cut through both the coarse-grained and fine-grained portions. The shock-induced melt veins have large variations in width from a few micrometers to ~2 mm. However, most of them are less than 200 μm in width. The shock-induced melt veins consist predominantly of fine-grained (usually <4 μm in size) clinopyroxene or garnet (Figs. 2 and 3). A few wide melt veins exhibit a zoning texture in mineral assemblage (Fig. 2a). The edge zone is dominated by fine-grained pyroxene, while in the central zone garnet is dominant with clinopyroxene and coesite as minor phase. Representative compositions of the fine-grained pyroxene and garnet in shock-induced melt veins are given in Table 2. The clinopyroxene grains have a low sum of cations (3.81–3.83) on the basis of six oxygen atoms, indicating high contents of cation vacancy. The garnet grains are super-silicic, with 3.03–3.09 apfu Si on the basis of 12 oxygen atoms. In some of the shock-induced melt veins, relict fragments of pyroxenes, plagioclase (now as fine-grained aggregates

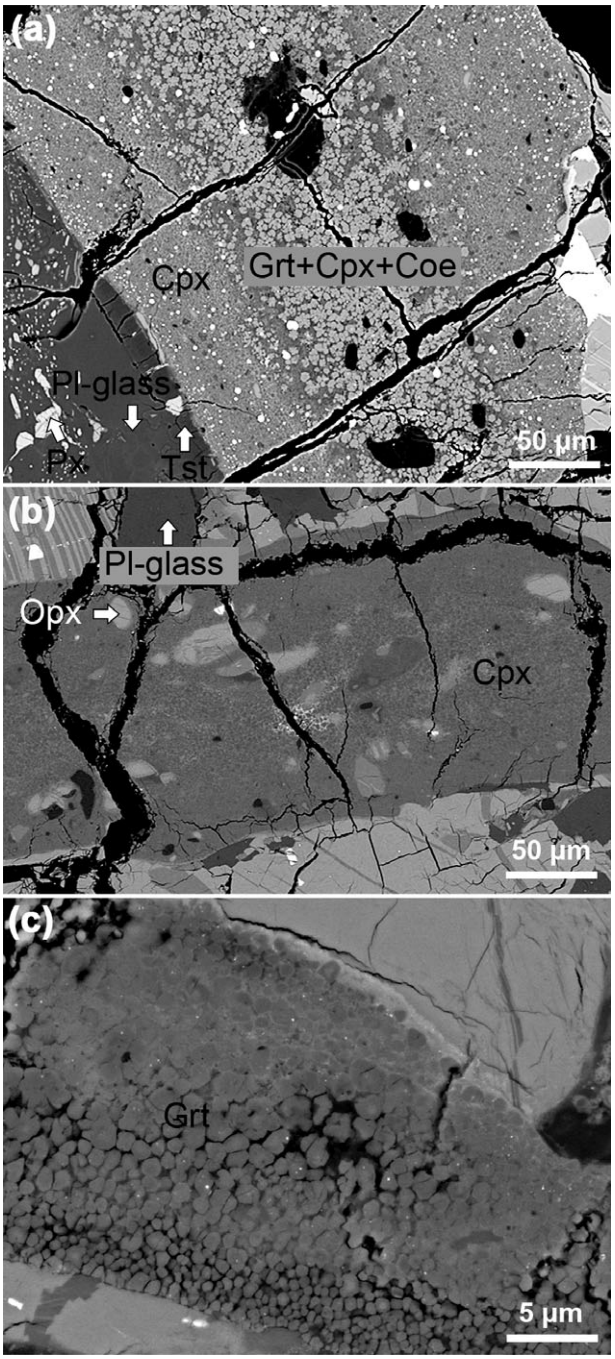

Fig. 2. Backscattered electron images of typical shock melt veins in NWA 2650. a) A shock-induced melt vein exhibits a zoning texture in mineral assemblage. b) The shock melt vein is dominated by clinopyroxene. c) The shock melt vein is dominated by super-silicic garnet. Px: pyroxene; Grt: garnet; Cpx: clinopyroxene; Tst = tissintite; Pl-glass = plagioclase glass; Opx = orthopyroxene; Coe = coesite.

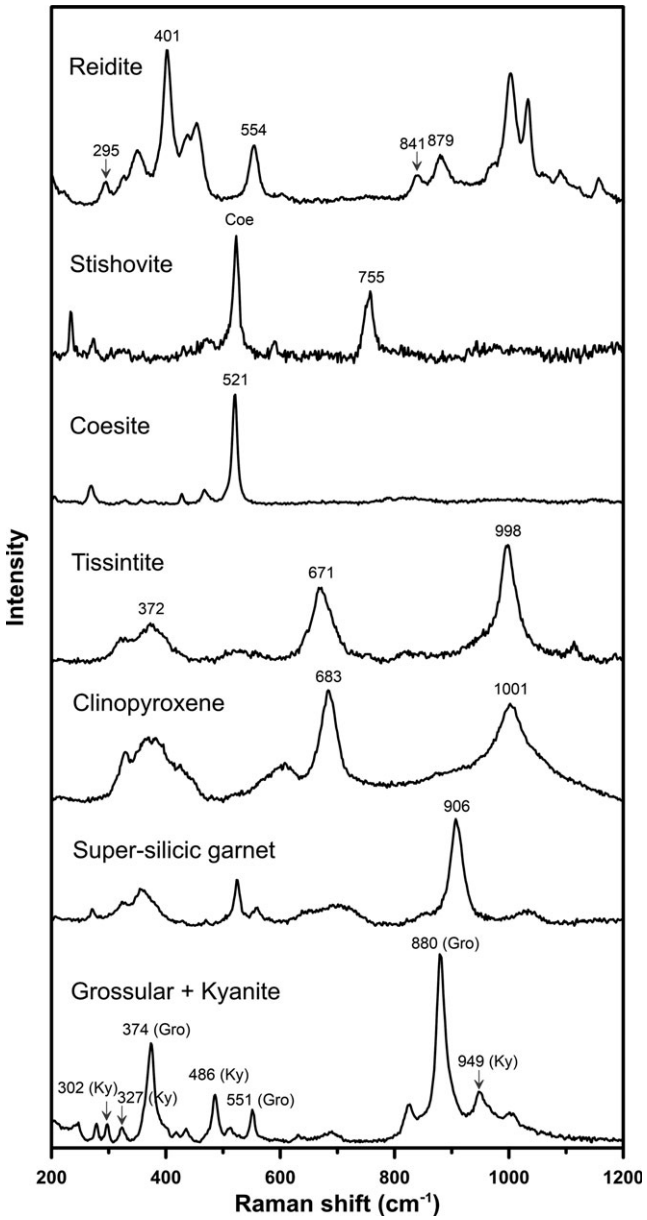

Fig. 3. Representative Raman spectra of minerals in NWA 2650 meteorite.

of tissintite, Figs. 4a and 4b), and silica phase (now as fine-grained aggregates of coesite and/or stishovite, Fig. 3) are observed (Fig. 5). The grain sizes of tissintite, coesite, and stishovite in aggregates are usually less than 1 μm. In addition, a few zircon grains that are closely associated with ilmenite contain irregular and lamellae-shaped reidite (Figs. 3 and 6).

Most plagioclase grains that are far (>200 μm) from shock-induced melt veins show abundant planar or irregular fractures. Some of them show undulatory extinction. Most of these planar and irregular fractures do not penetrate into the surrounding pyroxene grains. In some of these plagioclase grains with fractures, fracture-poor glassy veins are observed. The extension orientation of the plagioclase glassy veins is

Table 2. Average compositions (wt%) of vacancy-rich clinopyroxene and super-silicic garnet in shock-induced melt veins from NWA 2650.

	Vacancy-rich clinopyroxene		Super-silicic garnet	
	Average (n = 8)	1SD	Average (n = 6)	1SD
SiO_2	47.9	0.60	40.1	0.32
TiO_2	0.78	0.20	0.92	0.07
Cr_2O_3	0.15	0.04	0.35	0.03
Al_2O_3	23.3	1.22	20.5	0.31
FeO	7.43	1.00	16.4	0.36
MnO	0.25	0.04	0.58	0.03
MgO	3.45	0.53	7.04	0.14
CaO	14.9	0.46	13.6	0.16
Na_2O	1.37	0.15	0.48	0.03
K_2O	0.06	0.02	bdl	
Total	99.59		100.1	
Si	1.719		3.047	
Ti	0.021		0.052	
Cr	0.004		0.021	
Al	0.984		1.833	
Fe	0.222		1.038	
Mn	0.008		0.037	
Mg	0.186		0.802	
Ca	0.573		1.107	
Na	0.095		0.071	
K	0.003		0.000	
Total	3.815		8.009	

Bdl = below detection limit.
The cations in vacancy-rich clinopyroxene and super-silicic garnet are calculated based on 6 and 12 oxygen atoms, respectively.

generally parallel to those of shock-induced melt veins (Fig. 7a). In BSE images, these fracture-poor veins are brighter than the surrounding regions with abundant fractures. The width of the fracture-poor veins varies from a few tens of micrometers to over two hundreds of micrometers. In a few of these plagioclase glassy veins, elongate mineral fragments (up to ~110 μm in length) are present along the extension direction of the veins. Most of these fragments are aggregates of fine-grained tissintite (~200 nm) and contain small pyroxene grains (1–10 μm in size) (Fig. 7b). The empirical formula of the tissintite is $(Ca_{0.650}Na_{0.096}K_{0.005}Al_{0.972}Fe_{0.021}Mg_{0.010}Vacancy_{0.246})_{\Sigma=2}(Si_{1.619}Al_{0.381})_{\Sigma=2}O_6$. Some of the tissintite aggregates are closely associated with pyroxene grains, which have complex compositions (enriched in Mg, Fe, Al, and Ca; Fig. 7c). It is noteworthy that spherical troilite grains are also present in one of these fracture-poor regions of plagioclase (Fig. 7d).

Most of the plagioclase grains adjacent to shock-induced melt veins have been partially amorphized (Fig. 8a). Only a few plagioclase grains have been completely amorphous. These amorphous regions are usually fracture-free or fracture-poor. Some of them contain schlieren of molten pyroxene (Fig. 8b). Small vesicles (<10 μm) are observed along the boundaries between the plagioclase glass and pyroxene (Fig. 8b). A few plagioclase grains that are adjacent to the plagioclase glass contain parallel planar features (Fig. 8c). These planar features contain plagioclase glass and the spacing of the planar features ranges from 0.5 to 3 μm. They might be planar deformation features (PDFs). In some regions, pyroxene grains in direct contact with amorphous plagioclase exhibit radiating cracks (Fig. 8d). However, such plagioclase glasses are relatively rare in NWA 2650 and don't contain molten pyroxene. Tissintite occurs as a zone along the contact boundary between shock-induced melt veins or along the interfaces with pyroxene grains (Fig. 8e). The width of tissintite zones varies from 1 to 20 μm. The composition of the tissintite along the shock-induced melt veins is generally similar to those in plagioclase glass veins (Table 3).

Most plagioclase entrained in shock-induced melt veins has been replaced by fine-grained aggregates of tissintite (Fig. 8f). In one of the shock-induced melt veins that are dominated by fine-grained garnet, an oval-shaped region (80 × 55 μm; Fig. 9a) with plagioclase composition has been observed. At low magnification, the oval-shaped region shows a dendritic texture. High-magnification image of the oval shaped region demonstrates at least two phases are present (Fig. 9b). Raman spectra from this region show characteristic peaks for grossular (374, 551, and 880 cm^{-1}) and kyanite (302, 327, 486, and 949 cm^{-1}) (Fig. 3). At the boundary between the oval-shaped region and the super-silicic garnet-dominant region, needle-like kyanite crystals (up to 2 μm in length) are observed in the interstitial glass among garnet grains. Grossular with a low Z-contrast grows on the bright super-silicic garnet grains (Fig. 9c). At the mantle portion of the oval-shaped region, columnar kyanite crystals fill the regions among different intergrowths of grossular and kyanite (Fig. 9d). At the central part, tissintite was detected based on its EBSD pattern. A FIB foil across the super-silicic garnet + glass region and the oval-shaped region was prepared. Combined EBSD pattern (Figs. 4c and 4d), TEM-EDS analyses (Fig. 10) and high resolution TEM observations (Fig. 11), the phases in the oval-shaped region are confirmed to be grossular, kyanite, and silica glass. Most of the grossular and kyanite grains are less than 500 nm in size. Figure 11 shows the elemental maps of the grossular + kyanite intergrowth region. Silica glass shows a diffuse diffraction pattern. It occurs as an interstitial phase, filling the regions between grossular and kyanite (Fig. 12a). No coesite and stishovite grains were detected in this oval-shaped region.

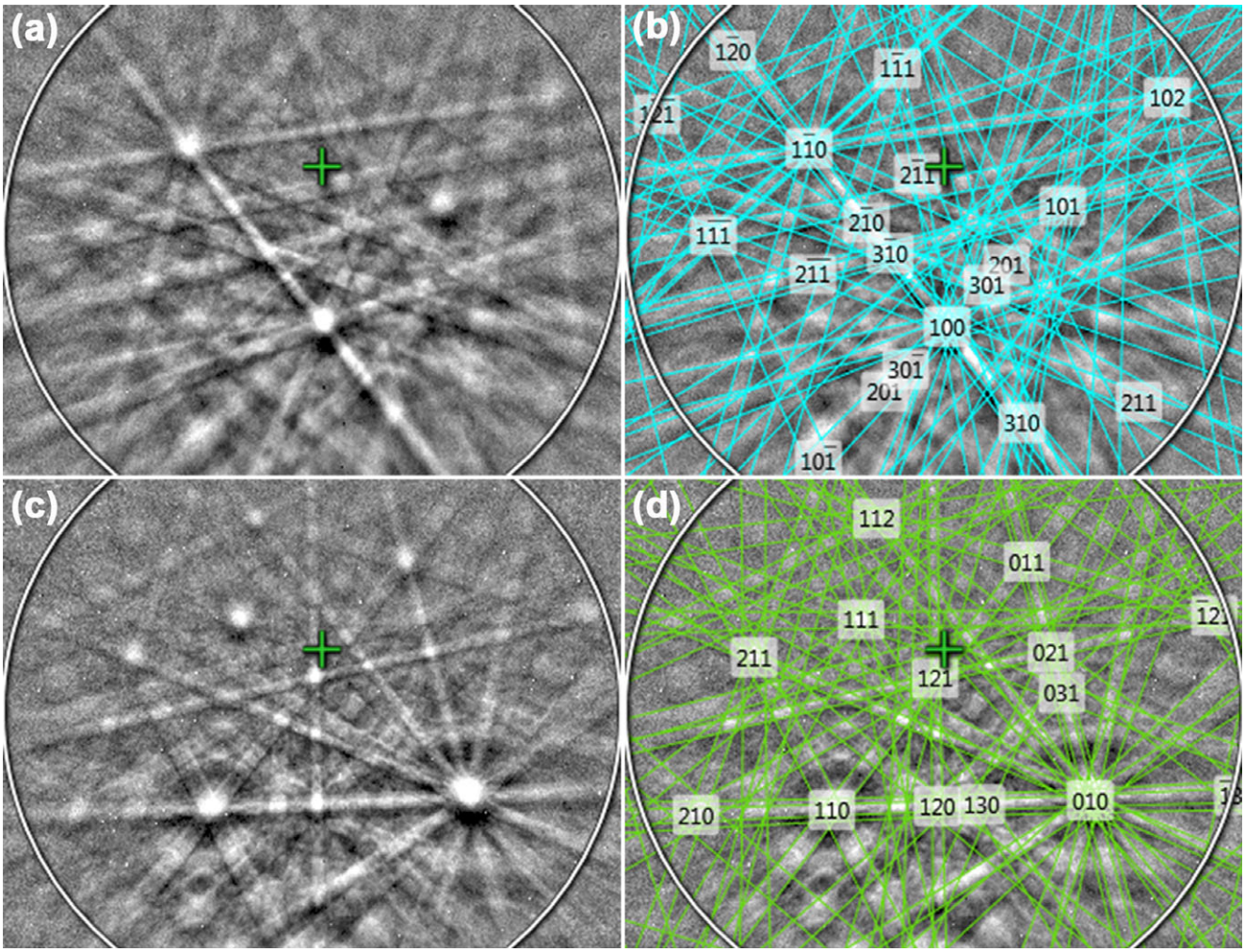

Fig. 4. EBSD patterns of tissintite (a and b) and grossular (c and d) in NWA 2650. a) EBSD pattern of tissintite in NWA 2650 and the pattern (b) indexed with the C2/c clinopyroxene structure (MAD = 0.47). c) EBSD pattern of grossular in NWA 2650 and the pattern (d) indexed with the grossular structure (MAD = 0.22).

DISCUSSION

Phase Transformation of Plagioclase

Plagioclase is one of the most important constituent minerals in NWA 2650. It shows diverse shock-induced features including planar and irregular fractures, undulatory extinction, amorphization, transformation into tissintite, and dissociation into three-phase assemblage of grossular + kyanite + silica glass. In this section, we will discuss their possible phase transformation mechanisms.

Conversion of Plagioclase into Glass

Plagioclase glasses in NWA 2650 can be divided into three groups based on their occurrences, including (1) vein-like plagioclase glasses far from shock-induced melt veins, (2) plagioclase glasses adjacent to shock-induced melt veins that are closely associated with untransformed plagioclase. Some of these plagioclase glasses contain a schlieren texture and vesicle along boundaries with surrounding pyroxene and (3) plagioclase glasses adjacent to shock-induced melt veins that are surrounded by radiating fractures in pyroxene. The former two groups are common; whereas the third occurrence is less common in NWA 2650.

Plagioclase glass has been widely observed in shocked terrestrial rocks and meteorites (Chen and El Goresy 2000; Jaret et al. 2015; and references therein). In the past decades, the plagioclase glasses in natural shocked samples are divided into diaplectic plagioclase glass and fused plagioclase glass. The former is suggested to have formed by solid-state transformation (Yamaguchi and Sekine 2000) whereas the latter formed by quenching after melting due to high postshock temperature, respectively (Jaret et al. 2015). The

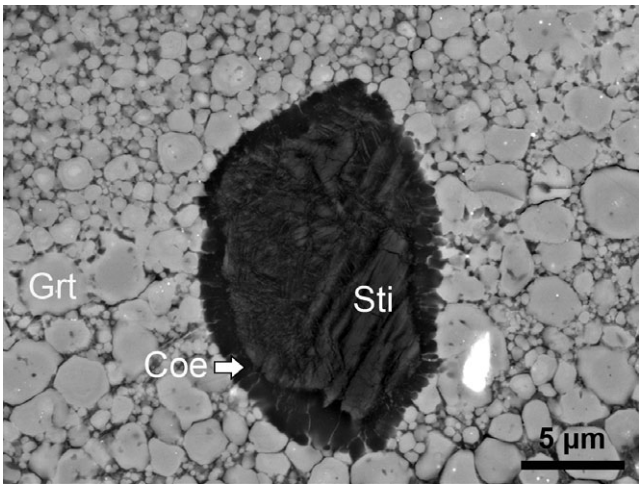

Fig. 5. Backscattered electron image of a fine-grained silica aggregate (coesite + stishovite) located in a super-silicic garnet-dominant shock melt vein. The silica aggregate contains a rim of granular coesite and a relatively large core of stishovite. Grt = garnet; Coe = coesite; Sti: stishovite.

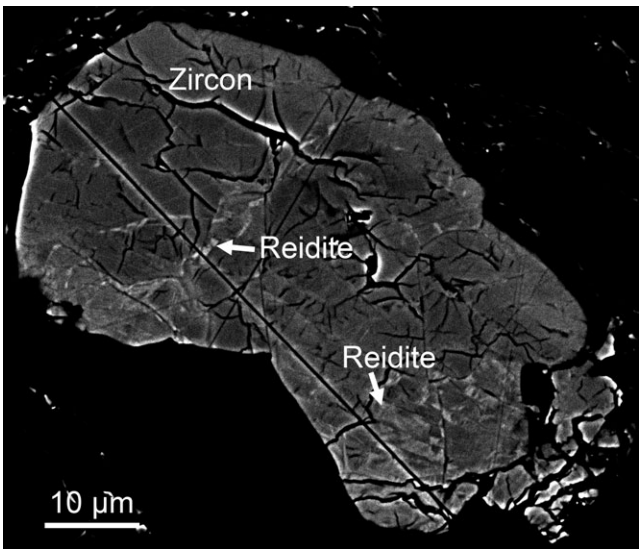

Fig. 6. Backscattered electron image of a zircon grain that has partially transformed into Reidite.

diaplectic glass was usually termed maskelynite. The diaplectic glass and the fused glass can be distinguished by their petrographic features. For example, the fused glass usually contains a schlieren texture and vesicles, which are absent in the diaplectic glass (Chen and El Goresy 2000). In addition, the diaplectic glass is usually associated with radiating fractures in surrounding silicate and oxide minerals. Chen and El Goresy (2000) proposed that diaplectic glass and maskelynite should have formed by different mechanisms. They suggested that maskelynite is derived from shock-induced melting and quenching at high pressure. The observations that support this viewpoint include the enrichment in potassium, deviation from stoichiometry, degradation of igneous zoning of precursor plagioclase, offshoots of maskelynite in pyroxene, and molten mesostasis and pyroxene (Chen and El Goresy 2000). The distinction between diaplectic glass and maskelynite remains blurred up to date. The usage of diaplectic glass and maskelynite in the literature usually is interchangeable and no nomenclature rules have been given or discussed. Given that the maskelynite grains in different investigations have a large variation of occurrence (e.g., Chen and El Goresy 2000; Jaret et al. 2015), we speculate that most of the diaplectic glasses and maskelynite grains have a common formation mechanism, i.e., via solid state transformation. The features that indicative of shock-induced melting in maskelynite grains could be result of local high postshock temperature. Future statistical investigations on the distribution of melting features in maskelynite are needed to check this inference.

According to the criteria of Chen and El Goresy (2000), the plagioclase glass that is enclosed by pyroxene with radiating fractures should be termed maskelynite. In NWA 2650, similar features can be observed. However, the plagioclase glass in such textural settings is restricted to the region that is in adjacent to shock-induced melt veins. This implies that temperature could also be an important factor for the transformation from plagioclase to maskelynite. Given no molten pyroxene or other features indicative of melting, we suggest that the maskelynite in NWA 2650 might have formed via solid-state transformation.

Most of the plagioclase glasses that are adjacent to shock-induced melt veins are closely associated with relict plagioclase grains. They are also not surrounded by radiating fractures. This textural feature indicates that these plagioclase glasses are not typical maskelynite, although the possibility that they are maskelynite or diaplectic glass cannot be completely excluded. However, many of these plagioclase glasses display a schlieren texture and contain vesicles along the boundaries with pyroxene grains, indicating that these plagioclase glasses have quenched from plagioclase melt. The schlieren texture and vesicles may have formed at different stages of the shock events. The schlieren texture might have formed during compression; whereas the vesicles have formed during pressure release (Chen and El Goresy 2000).

Different from the plagioclase glass discussed above and those documented in the literature (e.g., Chen and El Goresy 2000), vein-like plagioclase glass can be found within some plagioclase grains. The vein-like occurrence of these plagioclase glass indicates that a

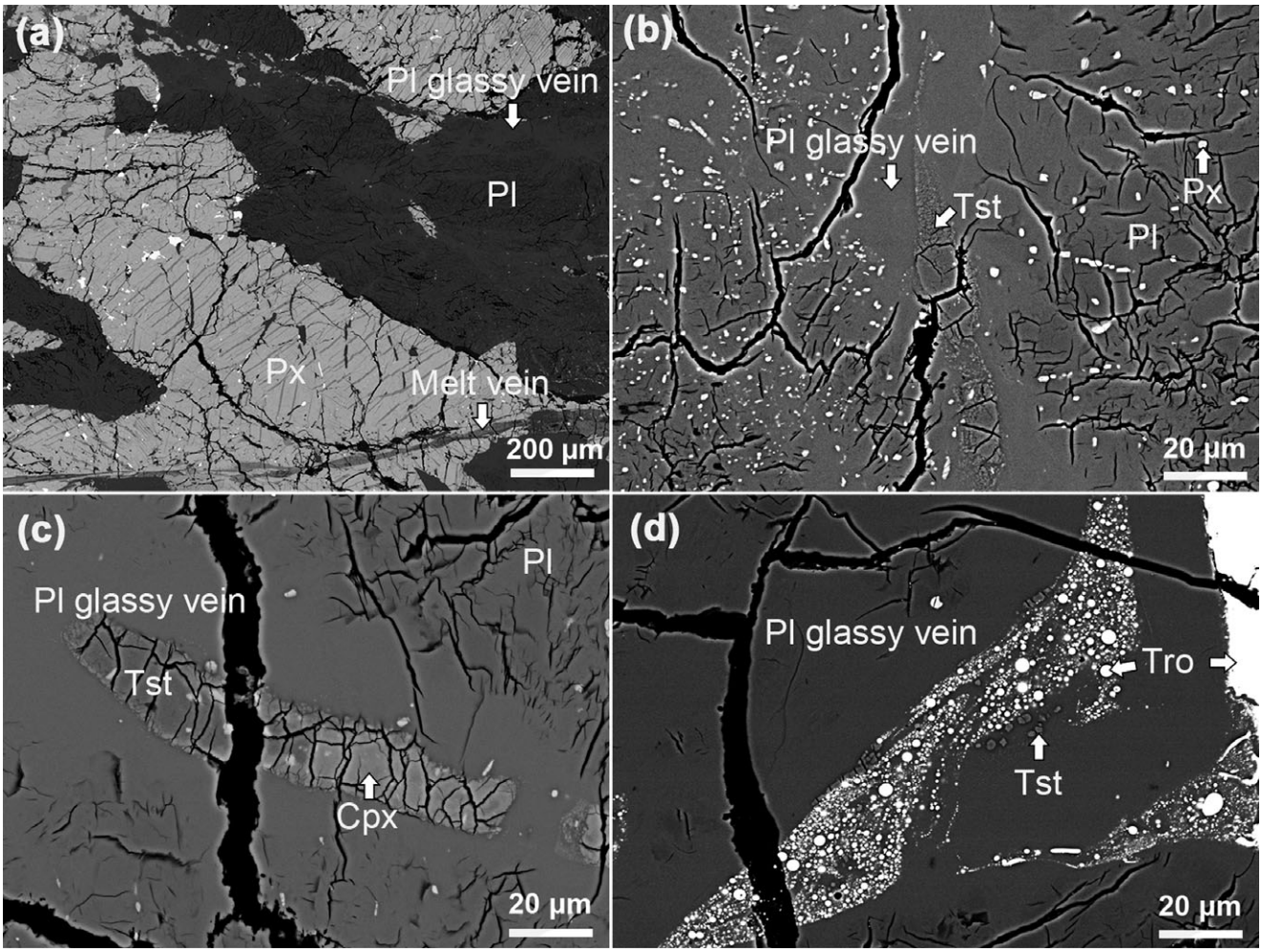

Fig. 7. Backscattered electron images of plagioclase glass veins. a) The extension orientation of the plagioclase glassy veins and shock-induced melt veins is generally parallel. b) The elongate distribution of fined-grained tissintite in a plagioclase glassy vein. c) Tissintite aggregates in a plagioclase glassy vein are closely associated with pyroxene grains. d) A plagioclase glassy vein contains rounded troilite grains. Pl = plagioclase; Px = pyroxene; Cpx = clinopyroxene; Tst = tissintite; Tro = troilite.

mechanism different from both diaplectic glass (maskelynite) and fused glass. Since the extension orientation of these glassy plagioclase veins are consistent with the normal shock-induced melt veins, we suggest that they might have formed by friction or shear melting, a mechanism similar to that for normal shock-induced melt veins (Gillet and El Goresy 2013). This inference is supported by the presence of spherical troilite grains in one of the plagioclase glassy veins, given that it is well known that the spherical shape of Fe-sulfide is mainly related to immiscibility between Fe-S and silicate melt.

Transformation of Anorthite into Tissintite

Tissintite is a recently found mineral with a composition of anorthitic plagioclase and a crystal structure of *C2*/*c* clinopyroxene (Ma et al. 2015). It has also been observed in the shocked eucrite NWA 8003 (Pang et al. 2016). Recently, tissintite has been synthesized with starting material of natural labradorite (Rucks et al. 2018). Rucks et al. (2018) revealed that tissintite could have formed from amorphous plagioclase but not crystalline plagioclase. In NWA 2650, three texturally different groups of tissintite have been observed, including: (1) tissintite aggregates in shock-induced melt veins, (2) tissintite in plagioclase glasses adjacent to shock-induced melt veins, and (3) tissintite aggregates in vein-like plagioclase glasses. As discussed above, the plagioclase glasses adjacent to shock-induced melt veins and vein-like plagioclase glasses have mainly formed by shock-induced melting and quenching. It is likely that the tissintite grains therein have crystallized from a plagioclase melt under pressure during decompression (cf. Rucks et al. 2018).

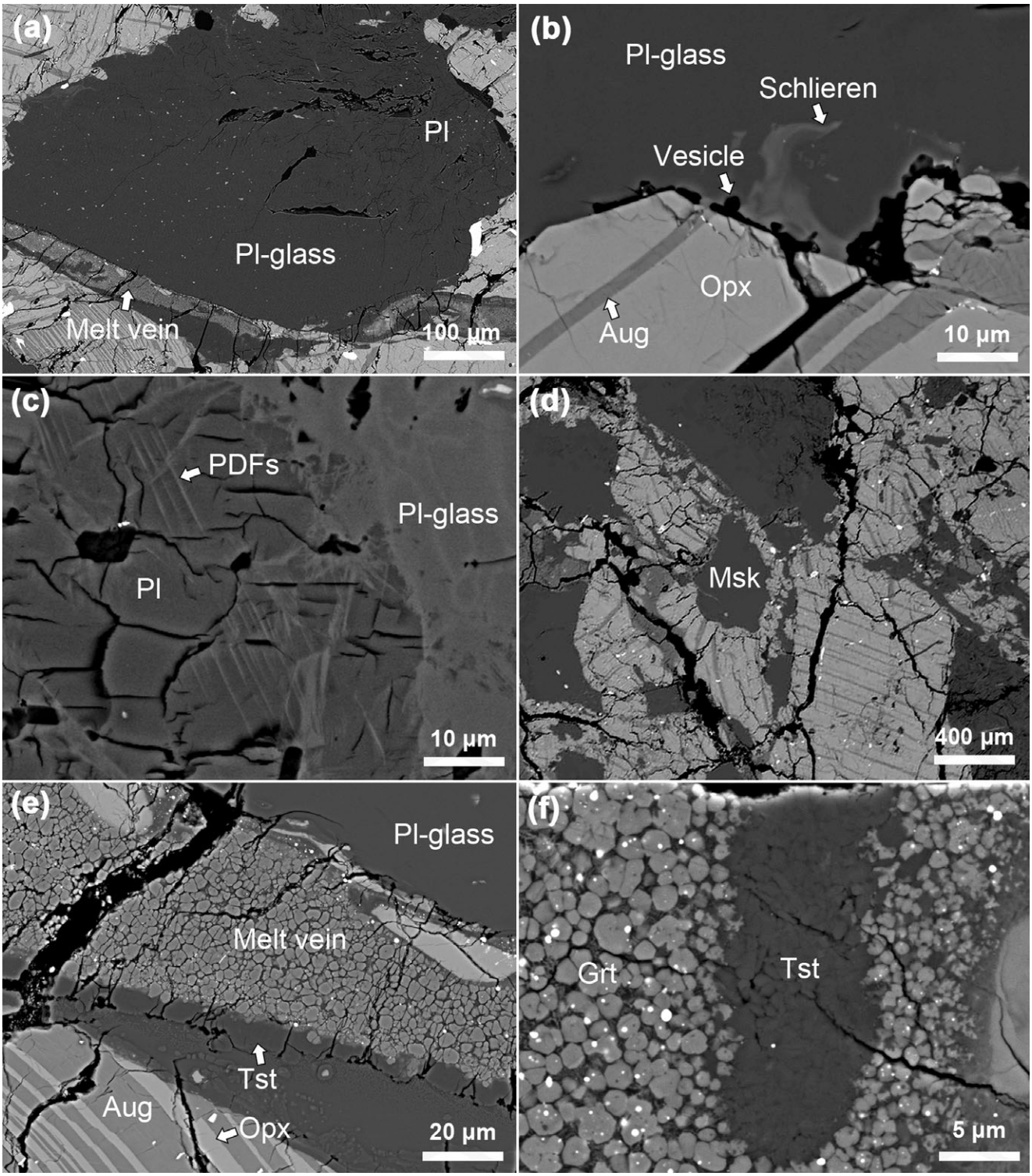

Fig. 8. Backscattered electron images of plagioclase glasses and tissintite. a) A large plagioclase grain has partially transformed into glass. b) A schlieren texture and vesicles occur at the boundary between plagioclase glass and pyroxene grain. c) A plagioclase grain adjacent to a shock melt vein contains PDFs, which are associated with plagioclase glass. d) A maskelynite adjacent to a shock melt vein is surrounded by radiating cracks in pyroxene. e) Tissintite occurs as a zone along the interfaces with the shock melt veins and along the interfaces with pyroxene grains. f) Fine-grained tissintite aggregates in shock melt vein. Grt = garnet; Tst = tissintite; Pl-glass = plagioclase glass; Pl = plagioclase; Aug = augite; Opx = orthopyroxene; Msk = maskelynite; PDFs = planar deformation features.

Table 3. Average compositions (wt%) of anorthite, tissintite, plagioclase glass, and maskelynite in NWA 2650.

	Anorthite in coarse-grained portion		Anorthite in fine-grained portion		Tissintite		Plagioclase glass		Maskelynite	
	Average (n = 8)	1SD	Average (n = 9)	1SD	Average (n = 14)	1SD	Average (n = 13)	1SD	Average (n = 9)	1SD
SiO_2	45.7	0.55	45.5	0.43	46.5	0.62	45.8	0.92	44.9	0.46
Al_2O_3	34.7	0.59	35.5	0.14	34.3	0.92	35.0	0.72	35.8	0.21
FeO	0.10	0.06	0.06	0.06	0.34	0.15	0.16	0.09	0.23	0.14
MgO	bdl	bdl	bdl	bdl	0.04	0.07	bdl	bdl	bdl	bdl
CaO	18.2	0.36	18.6	0.68	17.0	0.68	17.5	0.70	18.1	0.16
Na_2O	1.07	0.15	1.00	0.27	1.48	0.37	1.29	0.40	0.92	0.09
K_2O	0.06	0.02	0.04	0.02	0.11	0.04	0.07	0.03	0.05	0.01
Total	99.83		100.7		99.77		99.82		100.0	
Si	2.106		2.089		1.604					
Al	1.888		1.903		1.397					
Fe	0.004		0.002		0.010					
Mg	bdl		0.001		0.002					
Ca	0.901		0.917		0.630					
Na	0.095		0.089		0.099					
K	0.004		0.002		0.005					
Sum	4.999		5.005		3.748					
An	90.1		90.9							
Ab	9.5		8.9							
Or	0.4		0.2							

Bdl = below detection limit.
The cations in anorthite and tissintite are calculated based on eight and six oxygen atoms, respectively.

The small pyroxene grains in plagioclase glasses and early crystallized vacancy-rich clinopyroxene grains in shock-induced melt veins might have provided crystalline seeds for nucleation of tissintite. The tissintite aggregates in shock-induced melt veins might have also crystallized from a plagioclase melt; however, a solid-state transformation mechanism similar to the transition from olivine to ringwoodite cannot be totally excluded based on the observations in this study.

Transformation of Anorthite into Grossular + Kyanite + Silica Glass

Transformation of anorthite to three-phase assemblage of grossular + kyanite + silica has not been reported in shocked meteorites. However, Fudge et al. (2017) once detected the presence of grossular in the shocked eucrite NWA 10658 by Raman spectroscopy and electron backscatter diffraction. They have suggested that grossular might have formed by the reaction $3CaAl_2Si_2O_8 = Ca_3Al_2Si_3O_{12} + 2Al_2SiO_5 + SiO_2$ (Perkins et al. 1977; Fudge et al. 2017). However, no Al_2SiO_5 polymorphs and SiO_2 phases has been observed in Fudge et al. (2017). The Raman spectra and TEM observations in our study confirm this reaction. However, the petrographic textures imply that the three-phase assemblages might not be the products of solid-state decomposition of anorthite. Instead, they might have crystallized from a plagioclase melt under pressure. The evidence includes the presence of needle-shaped kyanite crystals, overgrowth of super-silicic garnet by grossular, and kyanite aggregates filling the interstitial regions.

Constraints on the Shock Pressure and Temperature in NWA 2650

Although abundant HED meteorites have been found, detailed mineralogical investigations of shock metamorphism have been carried out only for a few samples (Buchanan et al. 2005; Miyahara et al. 2014; Pang et al. 2016, 2018a, 2018b; Fudge et al. 2017; Liao and Hsu 2017). Up to date, NWA 2650 is one of the few shocked eucrites that contain diverse phenomena of shock metamorphism. High-pressure phases such as coesite and stishovite, vacancy-rich clinopyroxene, super-silicic garnet, reidite, maskelynite, tissintite, and the three-phase assemblage grossular-kyanite-silica glass have been observed. With these high-pressure phases, the shock pressure and temperature in NWA 2650 can be constrained.

Based on the phase diagram of silica (Zhang et al. 1993; Presnall 1995), the coexistence of coesite and stishovite indicates a shock pressure of 8–13 GPa with a wide range of temperature. However, given that the

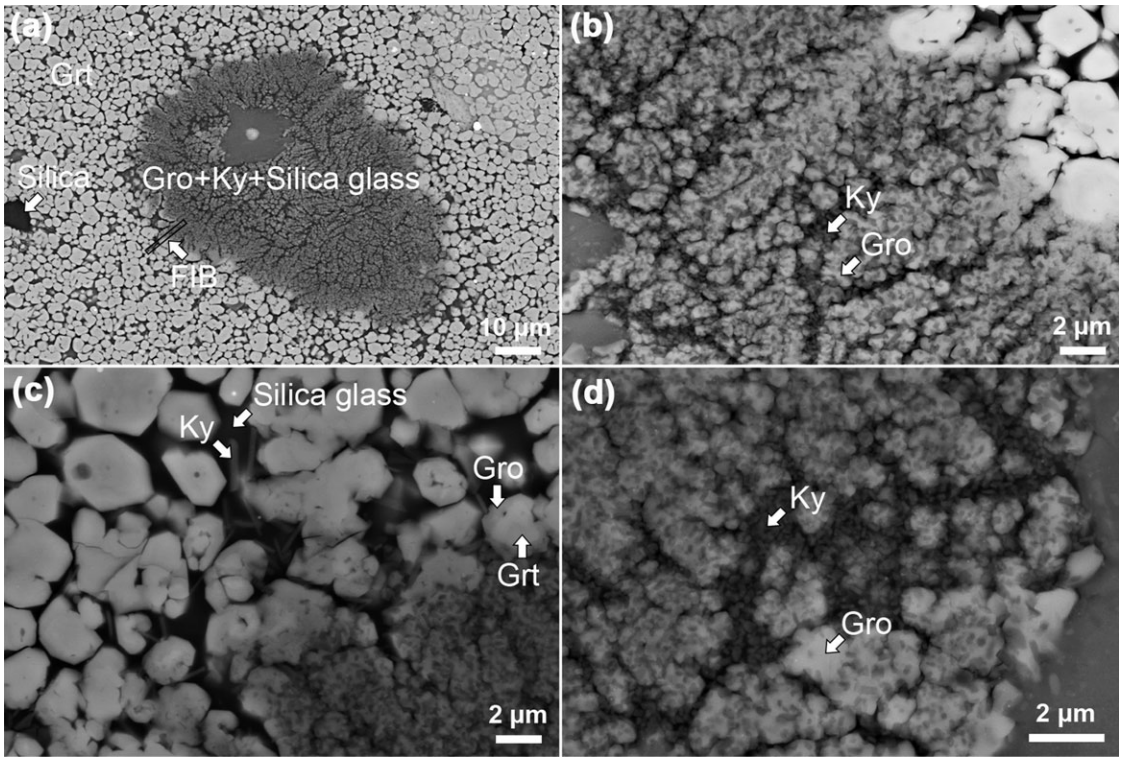

Fig. 9. Backscattered electron image of grossular + kyanite + silica glass minerals assemblage in NWA 2650. a) An oval-shaped region contains grossular, kyanite, and silica glass is surrounded by fine-grained super-silicic garnet. The position of a FIB foil is marked with black rectangle. b) A representative region of intergrowth of grossular and kyanite. c) Needle-like kyanite crystals occur in the glass among super-silicic garnet grains. d) Column kyanite crystals fill the regions among different intergrowths of grossular and kyanite. Grt: garnet; Gro = grossular; Ky = kyanite.

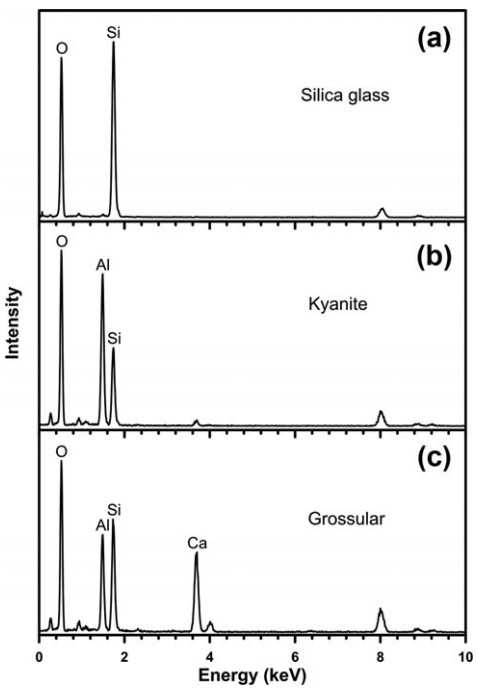

Fig. 10. TEM-EDS spectra of silica glass, kyanite, and grossular in the oval-shaped region shown in Fig. 9.

kinetic barrier for transformation from quartz to coesite is high, high temperature would be required to enhance the transformation. This is consistent with the petrographic observation that coesite mainly occurs along the boundary between silica aggregate and surrounding fine-grained minerals in melt veins (cf. Pang et al. 2016). The vacancy-rich clinopyroxene is the predominant phase in simple shock melt veins and occurs at the margin of the zoned shock melt veins. This indicates that the vacancy-rich clinopyroxene is an early phase crystallized from melt veins. However, vacancy-rich clinopyroxene has a wide stability field with pressure ranging from <2 to >20 GPa (Liu 1980). Given the complex composition of the vacancy-rich clinopyroxene compared with those in synthetic experiments, it is difficult to constrain the shock pressure and temperature based on the presence of vacancy-rich clinopyroxene in NWA 2650. The concentrations of Si and Al+Cr in super-silicic garnet are functions of pressure based on previous investigations (Aoki and Takahashi 2004). The maximum concentration of Si in super-silicic garnet is 3.09 apfu, indicating an upper limit pressure of approximately 8 GPa for the crystallization of super-

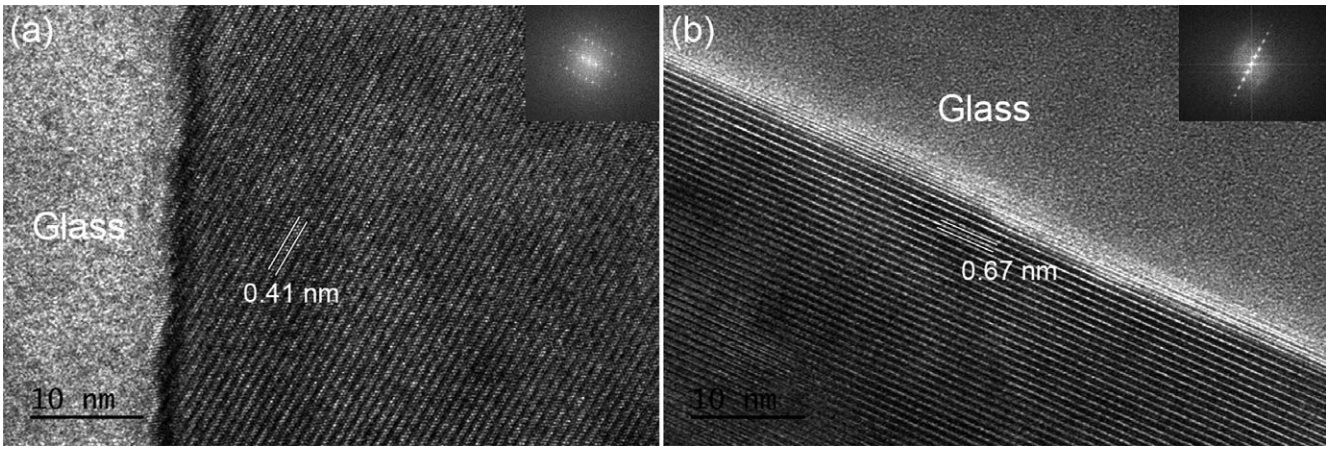

Fig. 11. High-resolution TEM images of grossular (a) and kyanite (b) in NWA 2650.

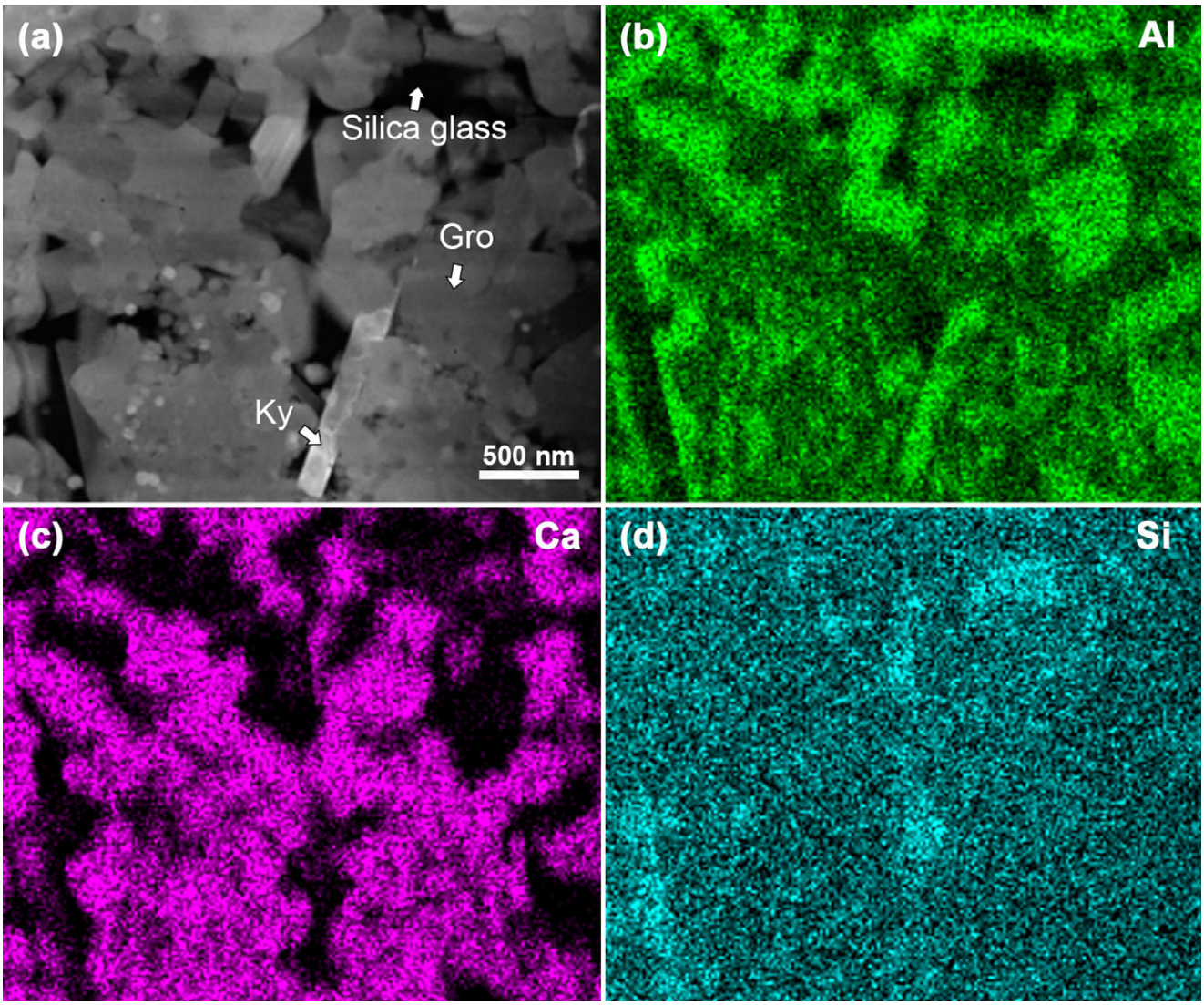

Fig. 12. HAADF-TEM image (a) and X-ray mapping results of Al (b), Ca (c), and Si (d) in the region consisting of grossular, kyanite, and silica glass. Gro = grossular; Ky = kyanite.

silicic garnet. This pressure is consistent with that inferred from the minimum Al+Cr concentration. Reidite is an important indicator of shock pressure (Wittmann et al. 2006). Zircon starts to transform into reidite at approximately 20 GPa through solid-state transformation (Fiske et al. 1994; Wittmann et al. 2006), although a shock pressure of approximately 30 GPa was also proposed (Kusaba et al. 1985; Chen et al. 2013; Timms et al. 2017). In NWA 2650, the lamellae-shaped texture of reidite indicates that it might also have formed through solid-state transformation. Therefore, the presence of reidite in NWA 2650 indicates a peak shock pressure of at least ~20 GPa.

Maskelynite is an important high-pressure phase in many shocked meteorites (e.g., ordinary chondrites, Martian meteorites, and lunar meteorites). Based on the recent study, maskelynite can have formed under pressure down to 17 GPa (Hu et al. 2017). However, different from most of the other high-pressure phases (except for reidite) in NWA 2650 that have crystallized from high-temperature and high-pressure melts, maskelynite has formed through a solid-state transformation. Therefore, the formation of maskelynite can only provide a clue to constrain the peak shock pressure in NWA 2650. Although tissintite has been observed in a few shocked Martian meteorites and eucrite meteorites, it was only synthesized in a recent shock experiment (Rucks et al. 2018). With starting material composition An_{60}, Rucks et al. (2018) has synthesized tissintite at 6–8.5 GPa and 1000–1350 °C. In NWA 2650, the shock pressure for the formation of tissintite might be similar to this pressure range, although a relatively lower pressure would be high enough for the stability of tissintite. The presence of assemblage grossular + kyanite + silica melt in NWA 2650 is its first description in shocked meteorites, although grossular and kyanite have been observed in shocked eucrites (Fudge et al. 2017; Pang et al. 2018b). Based on previous experimental results, the assemblage grossular + kyanite + silica has a large range of pressure and temperature (~2–15 GPa and < 2000 °C; Liu et al. 2012), with various pressure and temperatures corresponding to the species of silica. At relatively low temperature, the silica phase changes from quartz, to coesite, and to stishovite with increasing pressures (Liu et al. 2012). Silica melt that is coexisting with grossular and kyanite is only present at higher temperatures (up to 1600–2000 °C and 9–15 GPa). However, as we discussed above, grossular and kyanite are crystallization products from a plagioclase melt. Because some grossular grains overgrown on super-silicic garnet and some kyanite grains are present in the melt among super-silicic garnet grains, the formation of grossular and kyanite should postdate the crystallization of super-silicic garnet. Therefore, the pressure (probably >2 GPa) when grossular and kyanite crystallized should be lower than that for super-silicic garnet. The temperature should be higher than 1400 °C (Liu et al. 2012). Although the assemblage grossular + kyanite + silica melt has not been observed below ~9 GPa (Liu et al. 2012), the inference in this study is not in conflict with the high-P and high-T phase diagram of anorthite, in which the stability field of grossular + kyanite + silica melt remains unconstrained. To summarize, the presence of maskelynite and reidite probably indicates a minimum peak shock pressure up to 20 GPa, while the other high-pressure phases indicate that the shock pressure during the crystallization of shock melt veins might vary from >8 to >2 GPa with a heterogeneous temperature distribution.

Thermal History of NWA 2650

Although the meteorite NWA 2650 is a brecciated eucrite, pyroxene grains from the two portions with different grain size have identical compositions. This indicates that the two portions have a common source. Meanwhile, based on the compositions of augite and low-Ca pyroxene, the two-pyroxene thermometer gives an equilibrium temperature of 814 ± 33 °C. This might indicate that a basalt erupted on the surface of the eucrite parent body and then was buried probably by later erupted materials and experienced thermal metamorphism of 814 ± 33 °C. In addition, the fact that some shock-induced melt veins cut both the coarse-grained and fine-grained portions in NWA 2650 indicates that the shock metamorphism event postdated the fragmentation and brecciation event recorded in NWA 2650.

Acknowledgments—This work was financially supported by Natural Science Foundation of China (41673068) and Natural Science Foundation of Jiangsu Province of China (BK20170017). We thank two reviewers Dr. Steven Jaret and Dr. Chi Ma for their helpful reviews and Associate Editor Prof. Christian Koeberl for his editorial effort.

Editorial Handling—Dr. Christian Koeberl

REFERENCES

Aoki I. and Takahashi E. 2004. Density of MORB eclogite in the upper mantle. *Physics of the Earth and Planetary Interiors* 143–144:129–143.

Brey G. P. and Köhler T. 1990. Geothermobarometry in four-phase lherzolites II. New thermobarometers, and practical assessment of existing thermobarometers. *Journal of Petrology* 31:1353–1378.

Buchanan P. C., Noguchi T., Bogard D. D., Ebihara M., and Katayama I. 2005. Glass veins in the unequilibrated

eucrite Yamato 82202. *Geochimica et Cosmochimica Acta* 69:1883–1898.

Chen M. and El Goresy A. 2000. The nature of maskelynite in shocked meteorites: Not diaplectic glass but a glass quenched from shock-induced dense melt at high pressures. *Earth and Planetary Science Letters* 179:489–502.

Chen M., Yin F., Li X., Xie X., Xiao W., and Tan D. 2013. Natural occurrence of reidite in the Xiuyan crater of China. *Meteoritics & Planetary Science* 48:796–805.

Fiske P. S., Nellis W. J., and Sinha A. K. 1994. Shock-induced phase transitions of $ZrSiO_4$, reversion kinetics, and implications for terrestrial impact craters (abstract). *EOS Transactions* 75:416–417.

Fudge C., Hu J., Ma C., Wittmann A., and Sharp T. G. 2017. Shock induced feldspar and silica transformation in polymict eucrite Northwest Africa 10658 (abstract #2525). 48th Lunar and Planetary Science Conference. CD-ROM.

Gillet P. and El Goresy A. 2013. Shock events in the solar system: The message from minerals in terrestrial planets and asteroids. *Annual Review of Earth and Planetary Sciences* 41:257–285.

Hu J. P., Asimow P. D., and Liu Y. 2017. Low-pressure maskelynization of porous basalt: implications for basaltic achondrites and planetary impacts (abstract #1812). 48th Lunar and Planetary Science Conference. CD-ROM.

Jaret S. J., Woerner W. R., Phillips B. L., Ehm L., Nekvasi H., Wright S. P., and Glotch T. D. 2015. Maskelynite formation via solid-state transformation: Evidence of infrared and X-ray anisotropy. *Journal of Geophysical Research: Planets* 120:570–587.

Kubo T., Kimura M., Kato T., Nishi M., Tominaga A., Kikegawa T., and Funakoshi K. 2010. Plagioclase breakdown as an indicator for shock conditions of meteorites. *Nature Geoscience* 3:41–45.

Kusaba K., Syono Y., Kikuchi M., and Fukuoka K. 1985. Shock behavior of zircon: Phase transition to scheelite structure and decomposition. *Earth and Planetary Science Letters* 72:433–439.

Liao S. and Hsu W. 2017. The petrology and chronology of NWA 8009 impact melt breccia: Implication for early thermal and impact histories of Vesta. *Geochimica et Cosmochimica Acta* 204:159–178.

Liu L. G. 1980. Phase relations in the system diopside-jadeite at high pressures and high temperatures. *Earth and Planetary Science Letters* 47:398–402.

Liu X., Ohfuji H., Nishiyama N., He Q., Sanehira T., and Irifune T. 2012. High-P behavior of anorthite composition and some phase relations of the CaO-Al_2O_3-SiO_2 system to the lower mantle of the Earth, and their geophysical implications. *Journal of Geophysical Research* 117:B09205. https://doi.org/10.1029/2012JB009290.

Ma C. 2018. A closer look at shocked meteorites: Discovery of new high-pressure minerals. *American Mineralogist* 103:1521–1522.

Ma C., Tschauner O., Beckett J. R., Liu Y., Rossman G. R., Zhuravlev K., Prakapenka V., Dera P., and Taylor L. A. 2015. Tissintite (Ca, Na,□)$AlSi_2O_6$, a highly-defective, shock-induced, high-pressure clinopyroxene in the Tissint Martian meteorite. *Earth and Planetary Science Letters* 422:194–205.

Ma C., Tschauner O., Beckett J. R., Rossman G. R., Prescher C., Prakapenka V. B., Bechtel H. A., and MacDowell A. 2018. Liebermannite, $KAlSi_3O_8$, a new shock-metamorphic, high-pressure mineral from the Zagami Martian meteorite. *Meteoritics & Planetary Science* 53:50–61.

McSween H. Y. Jr, Mittlefehldt D. W., Beck A. B., Mayne R. G., and McCoy T. J. 2011. HED meteorite and their relationship to the geology of Vesta and Dawn mission. *Space Science Reviews* 163:141–174.

Miyahara M., Ohrani E., Yamaguchi A., Ozawa S., Sakai T., and Hirao N. 2014. Discovery of coesite and stishovite in eucrite. *Proceedings of the National Academy of Sciences* 111:10,939–10,942.

Pang R. L., Zhang A. C., Wang S. Z., Wang R. C., and Yurimoto H. 2016. High-pressure minerals in eucrite suggest a small source crater on Vesta. *Scientific Reports* 6: 26,063. https://doi.org/10.1038/srep26063.

Pang R. L., Harries D., Pollok K., Zhang A. C., and Langenhorst F. 2018a. Vestaite $(Ti^{4+}Fe^{2+})Ti^{4+}{}_3O_9$, a new mineral in the shocked eucrite Northwest Africa 8003. *American Mineralogist* 103:1502–1511.

Pang R. L., Harries D., Pollok K., Zhang A. C., and Langenhorst F. 2018b. Formation and implication of the titanium-rich shock melt pockets in eucrite Northwest Africa 8003 (abstract #6228). 81st Annual Meeting of the Meteoritical Society.

Perkins D., Essene E. J., Westrum E. F., and Wall V. J. 1977. Application of new thermodynamic data to grossular phase relations. *Contributions to Mineralogy and Petrology* 64:137–147.

Presnall D. C. 1995. Phase diagrams of Earth-forming minerals. *American Geophysical Union* 248–268.

Rucks M. J., Whitaker M. L., Glotch T. D., Parise J. B., Jaret S. J., Catalano T., and Dyar M. D. 2018. Making Tissintite: Mimicking Meteorites in the Multi-Anvil. *American Mineralogist* 103:1516–1519.

Sharp T. G. and DeCarli P. S. 2006. Shock effects in meteorites. *Meteorites and the Early Solar System* II:653–677.

Sharp T. G., Walton E. L., Hu J., and Agee C. 2019. Shock conditions recorded in NWA 8159 Martian augite basalt with implications for the impact cratering history on Mars. *Geochimica et Cosmochimica Acta* 246:197–212.

Sims M., Jaret S. J., Carl E., Rhymer B., Schrodt N., Mohrholz V., Smith J., Konopkova Z., Liermann H. P., Glotch T. D., and Ehm L. 2019. Pressure-induced amorphization in plagioclase feldspars: A time-resolved powder diffraction study during rapid compression. *Earth and Planetary Science Letters* 507:166–174.

Timms N. E., Erickson T. M., Pearce M. A., Cavosie A. J., Schmieder M., Tohver E., Reddy S. M., Zanetti M. R., Nemchin A. A., and Wittmann A. 2017. A pressure-temperature phase diagram for zircon at extreme conditions. *Earth-Science Reviews* 165:185–202.

Tomioka N. and Miyahara M. 2017. High-pressure minerals in shocked meteorites. *Meteoritics & Planetary Science* 52:2017–2039.

Tschauner O. and Ma C. 2017. Stöfflerite, IMA 2017-062. CNMNC Newsletter No. 39, October 2017, p. 1285; *Mineralogical Magazine* 81:1279–1286.

Walton E. L., Sharp T. G., Hu J., and Filiberto J. 2014. Heterogeneous mineral assemblages in Martian meteorite Tissint as a result a recent small impact event on Mars. *Geochimica et Cosmochimica Acta* 140:334–348.

Wang S. Z., Zhang A. C., Pang R. L., Li Y., and Chen J. N. 2019. Possible records of space weathering on Vesta: Case

study in a brecciated eucrite Northwest Africa 1109. *Meteoritics & Planetary Science*. https://doi.org/10.1111/maps.13254

Wittmann A., Kenkmann T., Schmitt R. T., and Stöffler D. 2006. Shock-metamorphosed zircon in terrestrial impact craters. *Meteoritics & Planetary Science* 41:433–454.

Yamaguchi A. and Sekine T. 2000. Monomineralic mobilization of plagioclase by shock: An experimental study. *Earth and Planetary Science Letters* 175:289–296.

Zhang J., Liebermann R. C., Gasparik T., Herzberg C. T., and Fei Y. 1993. Melting and subsolidus relations of SiO_2 at 9–14 GPa. *Journal of Geophysical Research* 98:19,785–19,793.